
Rainy: Unlocking Satellite Calibration for Deep Learning in Precipitation

Zhenyu Yu¹ Hanqing Chen² Mohd Yamani Idna Idris¹ Pei Wang^{*3}

Abstract

Precipitation plays a critical role in the Earth’s hydrological cycle, directly affecting ecosystems, agriculture, and water resource management. Accurate precipitation estimation and prediction are crucial for understanding climate dynamics, disaster preparedness, and environmental monitoring. In recent years, artificial intelligence (AI) has gained increasing attention in quantitative remote sensing (QRS), enabling more advanced data analysis and improving precipitation estimation accuracy. Although traditional methods have been widely used for precipitation estimation, they face limitations due to the difficulty of data acquisition and the challenge of capturing complex feature relationships. Furthermore, the lack of standardized multi-source satellite datasets, and in most cases, the exclusive reliance on station data, significantly hinders the effective application of advanced AI models. To address these challenges, we propose the *Rainy* dataset, a multi-source spatio-temporal dataset that integrates pure satellite data with station data, and propose *Taper Loss*, designed to fill the gap in tasks where only in-situ data is available without area-wide support. The *Rainy* dataset supports five main tasks: (1) satellite calibration, (2) precipitation event prediction, (3) precipitation level prediction, (4) spatiotemporal prediction, and (5) precipitation downscaling. For each task, we selected benchmark models and evaluation metrics to provide valuable references for researchers. Using precipitation as an example, the *Rainy* dataset and *Taper Loss* demonstrate the seamless collaboration between QRS and computer vision, offering data support for “AI for Science” in the field of QRS and providing valuable insights for interdisciplinary collaboration and integration.

1. Introduction

Precipitation is one of the most critical components of the Earth’s hydrological cycle, significantly impacting agriculture, ecosystems, and water resource management (Tsakiris

& Loucks, 2023; Wang et al., 2023). Accurate and timely estimation of precipitation is essential for climate change studies, disaster management, and environmental monitoring (Tsatsaris et al., 2021; Boluwade, 2020; Zhou & Liu, 2024). Quantitative Remote Sensing (QRS) plays a vital role in estimating various physical parameters, including precipitation, through the analysis of satellite data (Abdalzاهر et al., 2023). Traditionally, QRS methods rely on physical models and empirical algorithms, which, while effective in some cases, face challenges in handling complex, large-scale data due to their inherent assumptions and dependence on external parameters (Chen et al., 2022; Yuan et al., 2020).

Meanwhile, the field of Computer Vision (CV) has made rapid progress in recent years, fueled by deep learning algorithms and large datasets, leading to breakthroughs in image recognition, segmentation, and object detection tasks (Li et al., 2022). However, despite significant advancements in CV, its application in quantitative remote sensing remains limited (Messina & Modica, 2022). This is mainly due to the lack of publicly available datasets specifically tailored for QRS tasks. Moreover, remote sensing imagery (e.g., satellite and hyperspectral data) differs significantly from RGB images commonly used in CV, making it challenging to directly apply existing CV models to QRS tasks.

Motivation and existing problems. One of the primary obstacles in integrating quantitative remote sensing with computer vision is the *lack of standardized open datasets*, especially for quantitative tasks like precipitation estimation. In the QRS field, satellite data often require complex preprocessing steps, including atmospheric correction, geometric rectification, and cloud removal, to ensure data accuracy (Kucharczyk & Hugenholtz, 2021; Tmušić et al., 2020). These preprocessing steps vary between studies, leading to inconsistencies in data quality and model performance, hindering fair comparisons across different methods (Zhao et al., 2022; Schneider et al., 2010). Additionally, the issue of *regional heterogeneity*—where environmental conditions vary significantly across geographic regions—means that models trained on data from one region may not generalize well to others (Mahrad et al., 2020). This lack of comparability between datasets further limits algorithm generalization and the development of robust models (Gorelick et al., 2017).

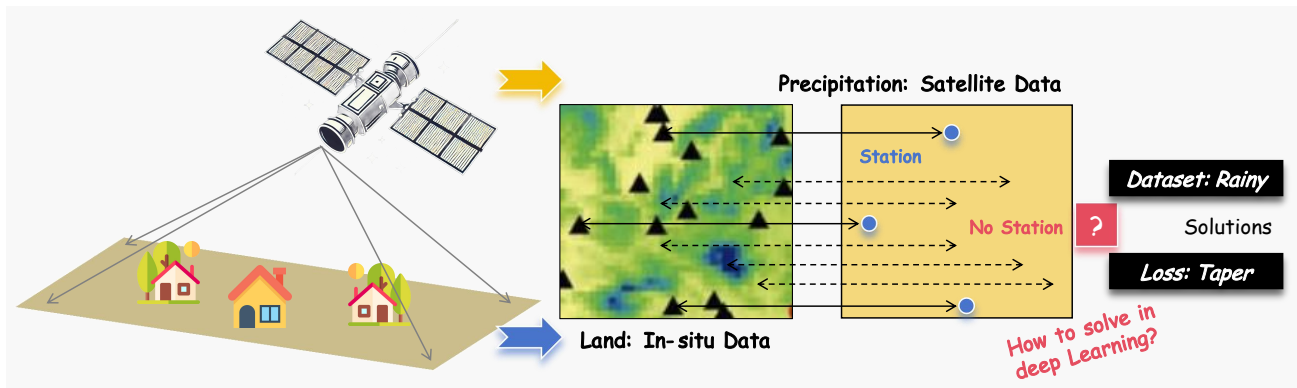


Figure 1. Motivation of this study. Satellite data provide wide coverage but lack ground-truth accuracy, while in-situ observations are sparse but reliable. The challenge is to integrate these data sources effectively for precipitation estimation. The proposed *Rainy* dataset and *Taper Loss* address this issue by leveraging deep learning to improve satellite calibration in regions with limited ground stations.

Combining satellite and in-situ data. In-situ data have the advantage of high accuracy and temporal resolution, providing precise local precipitation measurements but with limited spatial coverage (Kidd et al., 2020). In contrast, satellite data offer extensive spatial coverage with continuous observations over large areas, though they have relatively lower accuracy and resolution, often affected by atmospheric interference (Beck et al., 2017). Combining high-accuracy in-situ data with the broad coverage of satellite data can enable effective satellite calibration, achieving more accurate precipitation estimation (Le et al., 2023; Wu et al., 2020). Furthermore, deep learning algorithms have demonstrated strong performance in image recognition tasks, making them appealing for remote sensing applications like precipitation estimation. However, there is currently a lack of open datasets and tailored deep learning algorithms specifically designed to address the limitations posed by the scarcity of station data (Yuan et al., 2020; Moraux et al., 2019).

The main **contributions** of this work are as follows:

- We present *Rainy*, a publicly available dataset containing long-term, multi-source spatio-temporal data from both satellite and in-situ measurements. This dataset supports multiple tasks, including satellite calibration, event prediction, level prediction, spatio-temporal forecasting, and downscaling, providing benchmark data support for applying deep learning methods to satellite calibration in precipitation.
- We propose a novel loss function, *Taper Loss*, designed to prioritize reliable in-situ data during the matching and calibration process between satellite and ground data, thereby significantly improving validation accuracy. By applying a distance-weighted mechanism, this objective function effectively suitable for tasks lacking area-wide data support.

- We conduct experiments with various machine learning models and deep learning models, establishing a standardized **benchmark** for integrating CV models with QRS tasks and ensuring fair comparisons across different models and methods. This dataset facilitates model training and evaluation, promoting the development of AI applications tailored to QRS.

2. Related Work

2.1. Quantitative Remote Sensing

Quantitative remote sensing involves analyzing spectral, spatial, and temporal information in remote sensing images to estimate physical and environmental parameters such as vegetation indices, soil moisture, and surface temperature (Wu et al., 2019). Unlike qualitative analysis, quantitative remote sensing focuses on using mathematical models and physical equations to invert atmospheric and surface features, enabling precise monitoring and assessment of natural phenomena (Liang, 2005). It has been widely applied in fields such as climate change monitoring, ecological evaluation, and agricultural management (Dalei et al., 2021).

Satellite calibration is crucial in quantitative remote sensing to enhance the accuracy and reliability of satellite-derived measurements for applications such as climate monitoring, environmental analysis, and resource management (Xu et al., 2022). Calibration allows satellite data to closely align with ground-based observations by compensating for errors due to atmospheric conditions, sensor drift, and other environmental factors (Ma et al., 2021). However, satellite calibration faces several challenges, including the limited spatial and temporal resolution of data and the varying atmospheric conditions that affect data quality. These issues underscore the need for robust calibration methods in quantitative remote sensing.

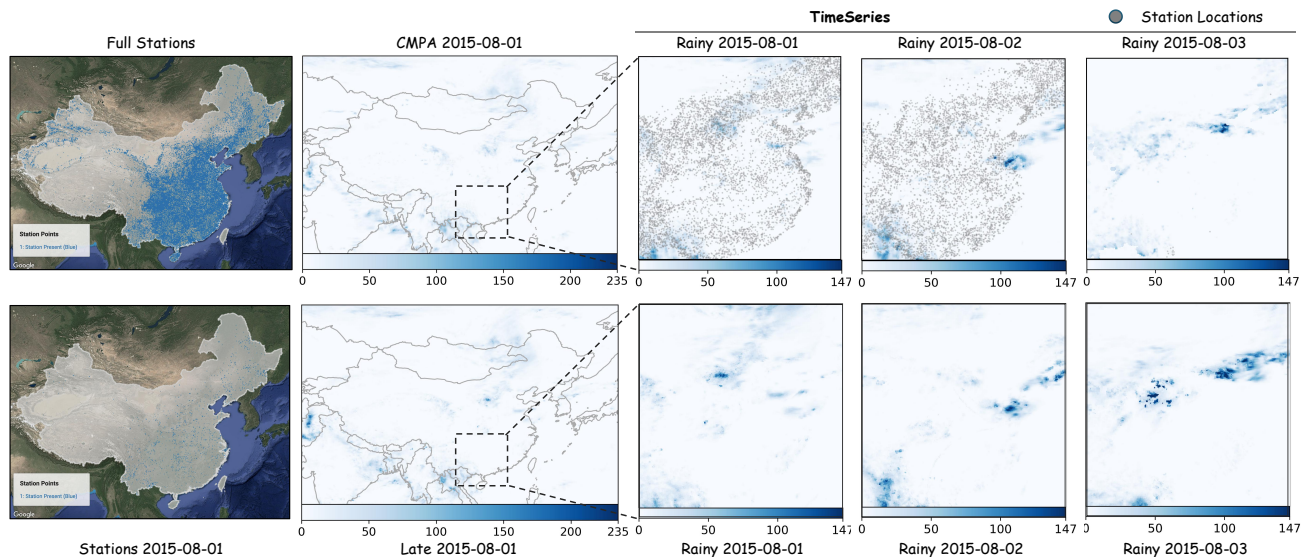


Figure 2. Overview of dataset *Rainy*, including CMPA, CMPA station, and Late data. The **full data** represents the complete precipitation dataset over China (440×700 pixels), while the **partial data** corresponds to a selected region from the *Rainy* dataset (256×256 pixels). This dataset is available in both daily and hourly versions, forming a long-term time series ($0.1^\circ/\text{pixel}$). The **full stations** dataset includes all stations across China from 2015 to 2017, though the specific stations corresponding to each data may vary. Notably, in CMPA data, only the stations provide accurate precipitation values. For certain time, CMPA data lacks station coverage, such as on August 3, 2015.

2.2. Traditional Methods

Traditional quantitative remote sensing methods primarily rely on physical and empirical models. Radiative Transfer Models (RTMs) are typical examples of physical models used to simulate the propagation of electromagnetic radiation through the atmosphere and surface, enabling the retrieval of surface characteristics (Himeur et al., 2022; Cheng et al., 2020). Empirical models, such as Vegetation Indices (VIs), estimate surface vegetation cover based on the ratio of near-infrared to red reflectance (Spadoni et al., 2020; Liu et al., 2020).

Despite their utility in specific scenarios, these methods face several challenges. **Parameter dependence:** Physical models require precise input parameters, such as atmospheric composition, topography, and vegetation distribution. The uncertainty in these parameters can significantly impact retrieval accuracy, and they are often difficult to measure or acquire (Pu & Gong, 2000; Singh et al., 2020). **Limited generalization:** Many empirical models heavily depend on monitoring data, performing well in calibrated regions but often struggling to generalize to other geographical areas with different environmental conditions. **High cost of acquiring monitoring data:** Establishing monitoring stations requires significant human and material resources, and it cannot compensate for the lack of historical observation data. **Complex data processing:** Traditional methods demand extensive data processing, especially for high-dimensional multispectral or hyperspectral data, leading to increased

computational costs (Liu et al., 2020).

2.3. Machine Learning Methods

In recent years, data-driven methods have gradually supplanted traditional models, with significant progress made in the application of machine learning (ML) and deep learning (DL) techniques in quantitative remote sensing. Models such as Support Vector Machines (SVM) (Cervantes et al., 2020), Random Forests (RF) (Antoniadis et al., 2021), and k-Nearest Neighbors (k-NN) (Bansal et al., 2022) have been applied to handle high-dimensional remote sensing data and capture complex nonlinear relationships (Diaz-Gonzalez et al., 2022; Prodhan et al., 2022). However, these ML models rely heavily on feature engineering and face challenges in scalability and computational efficiency as remote sensing datasets continue to grow. Additionally, while deep learning methods (e.g., LSTM (Hochreiter, 1997), ConvLSTM (Sainath et al., 2015), UNet (Ronneberger et al., 2015)) can automatically learn features, they require large amounts of labeled data and often struggle with generalization across different regions and sensor types (Ma et al., 2019; Li et al., 2022).

2.4. Integrating Computer Vision with Quantitative Remote Sensing

Integrating computer vision (CV) with QRS presents both opportunities and challenges. The primary challenge is the **data problem**. Unlike CV, which benefits from standardized

Table 1. Overview of the IMERG-Late and CMPA data products used in the *Rainy* dataset (2015-2017).

Data Product	Source	Spatial Resolution	Temporal Resolution	Coverage Area
IMERG-Late	GPM (Global Precipitation Measurement)	0.1°	30 minutes	Global
CMPA	China Meteorological Administration	0.05°	1 hour	China

datasets (e.g., ImageNet (Deng et al., 2009)), quantitative remote sensing lacks open datasets suitable for DL training and evaluation. Satellite data require extensive preprocessing (e.g., atmospheric correction, geometric rectification, and cloud removal (Abdelbaki & Udelhoven, 2022)), leading to inconsistencies across studies. Moreover, satellite data are highly **region-dependent**, making generalization across different geographic regions difficult.

Another challenge is **algorithm development**. Remote sensing data contain complex spatio-temporal information and multiple spectral channels, limiting the direct applicability of conventional CV models. Significant adaptation is required to transform in-situ and satellite data into meaningful supervisory signals for ML-based satellite calibration.

To address these challenges, a publicly available dataset with standardized preprocessing is essential for integrating CV with QRS. A well-structured dataset would enable fair benchmarking, foster robust algorithm development, and advance the field (Salcedo-Sanz et al., 2020).

3. Proposed Dataset - *Rainy*

3.1. Data Information

IMERG-Late (Integrated Multi-satellite Retrievals for GPM - Late Run) is a satellite-based precipitation product, merging microwave, infrared, and radar data to generate high spatiotemporal global precipitation estimates. IMERG-Late data are particularly useful for short-term precipitation forecasting and real-time event prediction.

CMPA (China Meteorological Administration Precipitation Analysis) is a high-resolution precipitation product that integrates ground-based and satellite data, developed specifically for China. CMPA enhances the precision of regional precipitation estimates and helps calibrate satellite-based precipitation data, ensuring higher accuracy in localized analyses.

These datasets provide essential references for precipitation estimation, supporting both regional and global-scale analysis. Data information can be found in Table 1. Temporal and spatial distribution is shown in Figure 2.

3.2. Supported Tasks

Task 1: Satellite calibration. Satellite calibration for precipitation involves estimating actual precipitation in a region using satellite data. Due to differences in sensor measure-

ments, satellite data must be calibrated against ground station data. This task is framed as a regression problem, where the model learns the relationship between satellite data and ground observations to improve precipitation estimation accuracy. This is the **primary task**, which involves calibrating satellite data using *Taper Loss* and station data.

Task Type: Regression

Objective: Precipitation amount (unit: mm)

Benchmark Models: RFR (Segal, 2004), BPANN (Hecht-Nielsen, 1992), XGBoost (Chen, 2015), MLP (Gardner & Dorling, 1998), LSTM (Hochreiter, 1997), UNet (Ronneberger et al., 2015), and ConvLSTM (Sainath et al., 2015).

Task 2: Precipitation event prediction. The goal of precipitation event prediction is to determine whether it will rain in a specific region. Due to the nature of satellite data, where each pixel represents a geographical area, this task is a binary classification problem that predicts whether precipitation will occur in the region. The task requires accurately identifying precipitation events across a wide spatial area.

Task Type: Binary classification

Objective: Will it rain (0-No / 1-Yes)

Benchmark Models: RF (Breiman, 2001), MLP (Gardner & Dorling, 1998), BPANN (Hecht-Nielsen, 1992), and LSTM (Hochreiter, 1997).

Task 3: Precipitation level prediction. The goal of precipitation level prediction is to classify precipitation into different levels based on the amount of rainfall. The precipitation level standards are detailed in Appendix. This is a multi-class classification problem, where the model predicts the precipitation intensity for a given region based on input satellite data.

Task Type: Multi-class classification

Objective: Precipitation level (0-No rain / 1-Light rain / 2-Moderate rain / 3-Heavy rain / 4-Storm / 5-Severe storm / 6-Extraordinary storm). The level standards are shown in Table.

Benchmark Models: RF (Breiman, 2001), MLP (Gardner & Dorling, 1998), BPANN (Hecht-Nielsen, 1992), and LSTM (Hochreiter, 1997).

Task 4: Spatiotemporal prediction. Spatiotemporal prediction of precipitation aims to forecast the distribution of precipitation over time. This task requires capturing both spatial and temporal dynamics, making it a spatiotemporal prediction problem.

Task Type: Spatio-temporal prediction

Table 2. Statistics for dataset *Rainy*. In (b), values displayed as 0.00 are rounded, but the actual values are near zero, not exactly zero. We selected 0.00 as the minimum and 6.22 (hourly) / 38.48 (daily) as the maximum (**bold**) for normalization. The normalization formula is $x' = \frac{x - x_{\min}}{x_{\max} - x_{\min}}$, where x , x_{\min} , x_{\max} , and x' represent the original value, minimum, maximum, and normalized value, respectively.

(a) Unfiltered data with all values included.

Hourly	Min	Max	Avg	Q1	Q2	Q3	Q99	Daily	Min	Max	Avg	Q1	Q2	Q3	Q99
CMPA	0.00	322.60	0.09	0.00	0.00	0.00	1.52	CMPA	0.00	761.15	1.90	0.00	0.00	0.11	23.25
Late	0.00	120.00	0.12	0.00	0.00	0.00	2.11	Late	0.00	863.20	2.88	0.00	0.03	1.07	32.31
All	0.00	322.60	0.11	0.00	0.00	0.00	1.81	All	0.00	863.20	2.39	0.00	0.00	0.44	27.27

(b) Data after removing zero values.

Hourly	Min	Max	Avg	Q1	Q2	Q3	Q99	Daily	Min	Max	Avg	Q1	Q2	Q3	Q99
CMPA	0.02	322.60	1.22	0.20	0.49	1.12	6.80	CMPA	0.02	761.15	6.92	0.49	1.98	6.58	37.25
Late	0.00	120.00	0.75	0.02	0.12	0.52	5.80	Late	0.00	863.20	5.07	0.08	0.63	3.43	40.29
All	0.00	322.60	0.90	0.08	0.26	0.77	6.22	All	0.00	863.20	5.67	0.22	1.15	4.84	38.48

Objective: Predict the future spatiotemporal distribution of precipitation across regions, incorporating both spatial patterns and temporal changes (unit: mm).

Benchmark Model: ConvLSTM (Sainath et al., 2015).

Task 5: Precipitation downscaling. Precipitation downscaling refers to the task of enhancing low-resolution satellite precipitation data to a higher resolution. This super-resolution reconstruction task typically relies on deep learning models to enhance spatial details and improve the resolution of precipitation data.

Task Type: Super-resolution reconstruction

Objective: Generate high-resolution precipitation data from low-resolution satellite observations to improve spatial accuracy and detail (unit: mm).

Benchmark Models: Bicubic (Parker, 2010), SRCNN (Dong et al., 2015), ESPCN (Shi et al., 2016), LapSRN (Lai et al., 2017), EDSR (Lim et al., 2017), ESRGAN (Wang et al., 2018), BSRGAN (Zhang et al., 2021), SwinIR (Liang et al., 2021), and DiffIR (Xia et al., 2023).

4. Method - Taper Loss

We propose *Taper Loss*, a novel loss function that incorporates distance-based weighting via kernel functions to minimize the error between sparse ground observation points and satellite image predictions. This loss function is designed to handle remote sensing tasks where ground observations are sparse and unevenly distributed, thereby improving model prediction accuracy.

Definition 4.1 (Satellite and ground data). Let $\mathbf{I}_1 \in \mathbb{R}^{M \times M}$ be the satellite data for the region of interest, and $\mathbf{I}_2 \in \mathbb{R}^{M \times M}$ be the ground observations, where only N points are reliable while the rest are interpolated with uncertainty.

Definition 4.2 (Reliable observation stations). Let $\{(x_1, y_1), (x_2, y_2), \dots, (x_N, y_N)\}$ represent the coordinates of N reliable ground observation points, with cor-

responding true values $\{z_1, z_2, \dots, z_N\}$.

Assumption 4.3 (Sparse observations). Due to the sparse distribution of observation points, directly generating a continuous spatial distribution map leads to inaccuracies. To address this, we propose *Taper Loss*, a loss function that incorporates distance decay to focus on reliable data points and weights the loss based on proximity.

Definition 4.4 (Distance-based kernel function). Let d_j be the distance from the j -th reliable ground observation point to its nearest observation, defined as:

$$d_j = d(x_j, y_j) \quad (1)$$

The distance-based kernel function $K(d_j)$ weights each point’s error according to its distance. Common kernel functions include:

$$K(d_j) = \begin{cases} e^{-\alpha d_j}, & \text{(Exponential decay kernel)} \\ \max(0, 1 - \beta d_j), & \text{(Linear decay kernel)} \\ \frac{1}{d_j^\gamma}, & \text{(Power-law decay kernel)} \\ e^{-\frac{d_j^2}{2\sigma^2}}, & \text{(Gaussian decay kernel)} \end{cases} \quad (2)$$

The choice of kernel function can be tailored based on the specific requirements of the task to capture different types of distance decay behavior.

Theorem 4.5 (Taper loss function). *The Taper Loss is defined as a weighted mean squared error, where the kernel function $K(d_j)$ down-weights the influence of interpolated points, focusing on minimizing the error at reliable points:*

$$\mathcal{L}_{\text{Taper}} = \sum_{j=1}^N K(d_j) \cdot (\mathbf{I}_1(x_j, y_j) - z_j)^2. \quad (3)$$

where $K(d_j)$ is the kernel function weighting the error based on the distance d_j to the nearest reliable observation. (x_j, y_j) represents the coordinates of the j -th reliable

ground observation point, with $\mathbf{I}_1(x_j, y_j)$ as the predicted value from the satellite image and z_j as the corresponding true observation value.

Remark 4.6 (Normalization for multiple reliable points). To ensure balanced contributions from multiple reliable observation points, we introduce a normalization factor to prevent any single point from dominating the loss calculation. The normalized *Taper Loss* is defined as:

$$\mathcal{L}_{\text{Taper, General}} = \sum_{j=1}^N \frac{K(d_j)}{\sum_{k=1}^N K(d_k)} \cdot (\mathbf{I}_1(x_j, y_j) - z_j)^2. \quad (4)$$

where $\sum_{k=1}^N K(d_k)$ is the normalization factor, ensuring balanced influence across observation points.

Theorem 4.7 (Optimization objective). *To minimize Taper Loss, we define the optimization objective with respect to model parameters θ as:*

$$\min_{\theta} \mathcal{L}_{\text{Taper}}(\theta) = \sum_{j=1}^N \frac{K(d_j)}{\sum_{k=1}^N K(d_k)} \cdot (\mathbf{I}_1(x_j, y_j; \theta) - z_j)^2. \quad (5)$$

By applying gradient descent or other optimization methods, the model can reduce errors in regions with reliable data while down-weighting the influence of less reliable areas.

Definition 4.8 (Total loss function). The total loss function combines *Taper Loss* with additional loss terms, formulated as:

$$\mathcal{L}_{\text{Total}} = \alpha \mathcal{L}_{\text{Taper}} + \beta \mathcal{L}_{\text{Other}}, \quad (6)$$

where $\mathcal{L}_{\text{Taper}}$ incorporates distance-based weighting to prioritize reliable observation points, and $\mathcal{L}_{\text{Other}}$ represents commonly used loss functions. In this work, we consider \mathcal{L}_1 (Mean Absolute Error) and \mathcal{L}_2 (Mean Squared Error) as examples. The hyperparameters α and β control the relative contributions of the two terms. The hyperparameters α and β balance *Taper Loss* and other loss terms, with default values set to 1.

5. Benchmark

5.1. Experimental Settings

The experiments were conducted on a single NVIDIA GeForce RTX A100 GPU with 80 GB of memory. For each task and model, hyperparameters were tuned to optimize performance. All machine learning models are initialized with default parameters, except for UNet and ConvLSTM in **Tasks 1 to 4**, where the learning rate is set to 0.001, the batch size to 32, and the number of epochs to 100. For **Task 5**, we downsample the data to $2\times$ as low-resolution images, while the original data is used as high-resolution images. The learning rate is set to $1e-4$, the batch size to 16, and the number of epochs to 200. To ensure the reliability of the

experimental results, each experiment was run five times with different random seeds. If the standard deviations were all less than 0.05, then omitted for simplicity.

Due to the large range of precipitation values and the presence of many zero values, there is significant data imbalance (see Table 2). To address this, we opted not to use z-score or standard min-max normalization methods. Instead, we chose a 99th percentile (Q99) truncation normalization approach, which helps prevent low values from being overly diminished. The data for Task 5 is normalized to a range of 0-255 using the corresponding data’s minimum and maximum values. This task does not require consideration of the issue of excessive zero values.

5.2. Evaluation Metrics

For each task in the *Rainy* dataset, specific evaluation metrics are applied. **Task 1** is evaluated using mean squared error (MSE) (Chai & Draxler, 2014), mean absolute error (MAE) (Willmott & Matsuura, 2005), and the coefficient of determination (R^2) (Willmott et al., 2012). For **Task 2** and **Task 3**, standard classification metrics including Accuracy (Chicco & Jurman, 2020), Precision (Nasir et al., 2021), Recall (Kleyko et al., 2018), and F1-score (Chicco & Jurman, 2020) are used. **Task 4** employs RMSE (Chai & Draxler, 2014) and MAE to measure predictive accuracy. For **Task 5**, we adopt RMSE, MAE, peak signal-to-noise ratio (PSNR) (Hore & Ziou, 2010), and structural similarity index (SSIM) (Wang et al., 2004) to assess both numerical accuracy and reconstruction quality. It should be noted that for Task 1, we have other metrics to choose from, which are commonly used in the field of satellite sensor calibration, as shown in the Appendix.

5.3. Comparison in Different Tasks

For **Task 1 (Satellite calibration)**, as shown in Table 4, we evaluated models on both daily and hourly precipitation data. The results indicate that the UNet model combined with *Taper Loss* achieved the best performance, with significant improvements in MSE, MAE, and R^2 compared to other models. Specifically, UNet+ $\mathcal{L}_{\text{Taper}}$ outperformed other methods with an MSE of 0.1349 and 0.1174, MAE of 0.045 and 0.0179, and R^2 of 0.6339 and 0.5311 for daily and hourly data, respectively. The results demonstrate the effectiveness of using *Taper Loss* for satellite calibration tasks, particularly in improving model accuracy and robustness.

For **Task 2 and Task 3 (Precipitation event and level prediction)** (see Table 3), MLP achieved the highest accuracy and F1-score for both tasks, with slight variations between metrics. Specifically, MLP and BPANN performed competitively, with accuracies around 0.7181 for Task 2 and 0.6746 for Task 3. LSTM also exhibited strong performance, particularly in Precision and F1-score. These results suggest

Table 3. Comparison of different methods for Task 2 (Precipitation Event Prediction) and Task 3 (Precipitation Level Prediction). **Bold** values indicate the best performance, while underlined values represent the second-best results.

Method	Task 2				Task 3			
	Accuracy	Precision	Recall	F1 Score	Accuracy	Precision	Recall	F1 Score
RF	0.6936	0.6751	0.6936	0.6705	0.6405	0.5877	0.6405	0.6036
MLP	0.7181	<u>0.707</u>	0.7181	<u>0.7079</u>	0.6746	<u>0.5936</u>	0.6746	<u>0.6223</u>
BPANN	0.7181	0.7067	0.7181	0.7072	<u>0.6745</u>	0.5918	<u>0.6745</u>	0.6212
LSTM	<u>0.7178</u>	0.7075	<u>0.7178</u>	0.7088	0.6739	0.5997	0.6739	0.6316

that deep learning models such as MLP and LSTM are well-suited for precipitation classification tasks, offering robust generalization across different scenarios.

In **Task 4 (Spatiotemporal prediction)**, where spatiotemporal prediction was evaluated (see Table 5). Models using *Taper Loss* consistently outperformed those using \mathcal{L}_1 or \mathcal{L}_2 loss functions alone. The best results were obtained with $\mathcal{L}_{Taper} + \mathcal{L}_1$, achieving RMSE values of 0.2118 and 0.0958 and MAE values of 0.0666 and 0.0135 for daily and hourly data, respectively. These findings highlight the advantage of incorporating *Taper Loss* in spatiotemporal prediction, particularly in reducing errors and enhancing temporal consistency.

For **Task 5 (Downscaling)**, we conducted experiments on $2 \times$ downscaling (see Table 6). Among the evaluated models, DiffIR achieved the best performance, with an RMSE of 0.0533, MAE of 0.0061, PSNR of 35.5604, and SSIM of 0.9855. SwinIR also demonstrated competitive performance, closely following DiffIR in all metrics. Traditional methods such as Bicubic interpolation showed significantly lower performance compared to deep learning-based models like SwinIR and DiffIR. These results indicate that advanced deep learning models are highly effective for precipitation downscaling tasks, offering superior accuracy and image reconstruction quality.

Key Insights. The introduction of *Taper Loss* significantly enhances model performance in tasks involving satellite calibration and spatiotemporal prediction, demonstrating its robustness in scenarios with only in-situ data. Deep learning models such as UNet, LSTM, and MLP consistently outperform traditional methods in both regression and classification tasks, highlighting the importance of leveraging advanced models for precipitation estimation. For downscaling tasks, state-of-the-art models like DiffIR and SwinIR exhibit remarkable improvements in accuracy and reconstruction quality, underscoring the potential of deep learning in high-resolution precipitation prediction. Overall, the experimental results validate the effectiveness of the *Rainy* dataset and the proposed methods, providing a comprehensive benchmark for future research in quantitative remote sensing.

Table 4. Comparison of different methods for Task 1 (Satellite Calibration) on daily and hourly data. **Bold** indicates the best performance, while underlined represents the second-best results.

Method	Daily			Hourly		
	MSE	MAE	R ²	MSE	MAE	R ²
BPANN	0.1988	0.0497	0.4887	0.1788	0.0443	0.4367
LSTM	0.1982	0.0523	0.4899	0.1784	0.0463	0.4377
MLP	0.1986	0.0510	0.4892	0.1788	0.0446	0.4368
RFR	0.2952	0.0604	0.3897	0.2648	0.0529	0.3267
XGBoost	0.2022	0.0514	0.4811	0.1816	0.0452	0.4302
ConvLSTM	0.1713	0.0536	0.3883	0.1411	0.0472	0.3758
+ \mathcal{L}_{Taper}	0.1538	<u>0.0455</u>	0.5067	0.1317	0.0351	0.4948
UNet	<u>0.1429</u>	0.0468	<u>0.5733</u>	<u>0.1215</u>	<u>0.0204</u>	0.4736
+ \mathcal{L}_{Taper}	0.1349	0.0450	0.6339	0.1174	0.0179	0.5311

Table 5. Comparison of different loss functions for Task 4 (Spatiotemporal Precipitation Prediction) on daily and hourly data. **Bold** values indicate the best performance, while underlined values represent the second-best results.

Loss	Daily		Hourly	
	RMSE	MAE	RMSE	MAE
$\mathcal{L}_{Taper} + \mathcal{L}_2$	<u>0.2255</u>	<u>0.0754</u>	<u>0.0987</u>	<u>0.0162</u>
$\mathcal{L}_{Taper} + \mathcal{L}_1$	0.2118	0.0666	0.0958	0.0135

Table 6. Comparison of different methods for Task 5 (Precipitation Downscaling, $2 \times$). **Bold** values indicate the best performance, while underlined values represent the second-best results.

Method	RMSE	MAE	PSNR	SSIM
Bicubic	0.1621	0.0347	32.3905	0.9549
SRCNN	0.1275	0.0227	34.2102	0.9554
ESPCN	0.1174	0.0221	34.2533	0.9656
LapSRN	0.1075	0.0187	35.2267	0.9654
EDSR	0.0939	0.0134	34.3801	0.9775
ESRGAN	0.0879	0.0139	34.4451	0.9718
BSRGAN	0.0853	0.0114	35.0409	0.9745
SwinIR	<u>0.0634</u>	<u>0.0079</u>	<u>35.5452</u>	<u>0.9813</u>
DiffIR	0.0533	0.0061	35.5604	0.9855

5.4. Ablation Study

Kernel function analysis. Taking the satellite calibration task (Task 1) as an example, we analyze the impact of dif-

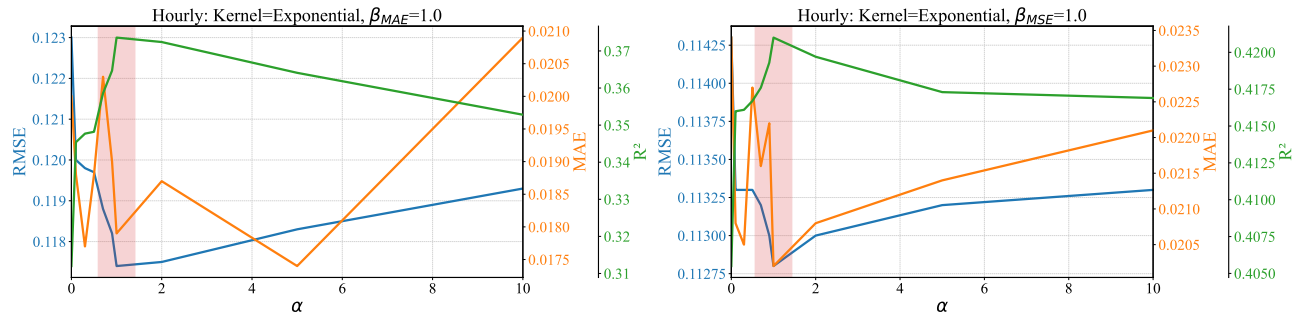


Figure 3. Ablation study of the *taper loss* parameter α for the Hourly Data, using Exponential function as examples, evaluating the impact on RMSE, MAE, and R^2 . The parameter β is set to 1.

ferent kernel functions under two types of loss functions: $\mathcal{L}_{Taper} + \mathcal{L}_1$ and $\mathcal{L}_{Taper} + \mathcal{L}_2$. Table ?? presents the comparison results for daily and hourly data across four kernel types: Exponential, Linear, Power-law, and Gaussian.

Daily data. Under $\mathcal{L}_{Taper} + \mathcal{L}_1$, the Exponential kernel achieves the best RMSE of 0.1349 ± 0.0049 and the highest R^2 of 0.6339 ± 0.0232 , demonstrating its superior capability in capturing spatial dependencies. For $\mathcal{L}_{Taper} + \mathcal{L}_2$, the Gaussian kernel performs best, with an RMSE of 0.133 ± 0.0029 and an R^2 of 0.642 ± 0.013 , indicating its robustness in modeling complex spatial relationships. The Power-law kernel shows higher RMSE and MAE values, particularly under $\mathcal{L}_{Taper} + \mathcal{L}_1$, indicating lower consistency in performance and higher sensitivity to parameter variations.

Hourly data. For hourly data, under $\mathcal{L}_{Taper} + \mathcal{L}_1$, the Exponential kernel again achieves the best performance, with an RMSE of 0.1174 ± 0.0016 , an MAE of 0.0179 ± 0.0012 , and an R^2 of 0.3736 ± 0.0179 . Under $\mathcal{L}_{Taper} + \mathcal{L}_2$, the Exponential kernel continues to perform well, achieving the lowest RMSE of 0.1128 ± 0.0004 and the highest R^2 of 0.421 ± 0.0042 . The Linear and Gaussian kernels show competitive performance, with slight variations in RMSE and MAE. Similar to daily data, the Power-law kernel exhibits the lowest consistency, confirming its sensitivity to parameter changes and its limited suitability for this task.

Analysis of taper loss parameter α . Figure 3, ??, and ?? illustrate the effect of the taper loss parameter α on model performance for hourly data, using the Exponential kernel as an example. We evaluate the impact of α on RMSE, MAE, and R^2 , with the parameter β fixed at 1.

For both daily and hourly datasets, smaller values of α ($\alpha < 2$) lead to unstable performance, with significant fluctuations in RMSE, MAE, and R^2 . This suggests that overly restrictive spatial tapering limits the model’s ability to generalize. At $\alpha = 1$, the model achieves the lowest RMSE and MAE, while R^2 approaches its peak, indicating that

$\alpha = 1$ is an optimal hyperparameter setting that effectively balances bias and variance. As α increases beyond 2, model performance stabilizes, showing that moderate tapering can maintain a good balance between bias and variance. Among all kernel functions, the Exponential and Gaussian kernels demonstrate smoother performance trends as α increases, whereas the Power-law kernel remains more sensitive to changes in α .

In all experiments, the weight parameter β for the \mathcal{L}_1 and \mathcal{L}_2 is fixed at 1, ensuring that \mathcal{L}_1 or \mathcal{L}_2 plays a primary role in optimizing the objective function. This fixed value ensures consistent and reliable comparison across different kernel functions and loss types.

6. Conclusion

The main contributions of this work include the introduction of the *Rainy* dataset and a novel loss function, *Taper Loss*, designed to advance the integration of computer vision (CV) models with quantitative remote sensing (QRS) tasks. The *Rainy* dataset integrates multi-source satellite data, including infrared, microwave, and radar observations, along with long-term ground station measurements, providing a comprehensive benchmark for spatio-temporal precipitation pattern analysis. By offering a standardized evaluation framework, *Rainy* facilitates fair comparison, robust model training, and the development of AI-driven solutions for QRS. Additionally, the proposed *Taper Loss* function effectively calibrates ground station data with spatial satellite observations, significantly improving the accuracy of loss calculation and model validation. This work represents a critical step in bridging the fields of CV and QRS, enabling more precise precipitation estimation and fostering innovative applications in environmental monitoring.

Impact Statement

This study introduces *Rainy*, a publicly available dataset based on deep learning, and proposes *Taper Loss*, a novel

approach to address the prediction challenges between station data and image data. The dataset is designed for five different spatiotemporal prediction tasks, including precipitation event prediction and precipitation estimation. The proposed dataset and method can be extended to a broader range of spatiotemporal forecasting applications, providing more accurate data support for environmental modeling and decision-making in weather-sensitive industries, thereby enhancing the reliability and practicality of meteorological predictions.

References

- Abdalzaher, M. S., Krichen, M., Yiltas-Kaplan, D., Ben Dhaou, I., and Adoni, W. Y. H. Early detection of earthquakes using iot and cloud infrastructure: A survey. *Sustainability*, 15(15):11713, 2023.
- Abdelbaki, A. and Udelhoven, T. A review of hybrid approaches for quantitative assessment of crop traits using optical remote sensing: research trends and future directions. *Remote Sensing*, 14(15):3515, 2022.
- Antoniadis, A., Lambert-Lacroix, S., and Poggi, J.-M. Random forests for global sensitivity analysis: A selective review. *Reliability Engineering & System Safety*, 206: 107312, 2021.
- Bansal, M., Goyal, A., and Choudhary, A. A comparative analysis of k-nearest neighbor, genetic, support vector machine, decision tree, and long short term memory algorithms in machine learning. *Decision Analytics Journal*, 3:100071, 2022.
- Beck, H. E., Van Dijk, A. I., Levizzani, V., Schellekens, J., Miralles, D. G., Martens, B., and De Roo, A. Mswep: 3-hourly 0.25 global gridded precipitation (1979–2015) by merging gauge, satellite, and reanalysis data. *Hydrology and Earth System Sciences*, 21(1):589–615, 2017.
- Boluwade, A. Remote sensed-based rainfall estimations over the east and west africa regions for disaster risk management. *ISPRS journal of photogrammetry and remote sensing*, 167:305–320, 2020.
- Breiman, L. Random forests. *Machine learning*, 45:5–32, 2001.
- Cervantes, J., Garcia-Lamont, F., Rodríguez-Mazahua, L., and Lopez, A. A comprehensive survey on support vector machine classification: Applications, challenges and trends. *Neurocomputing*, 408:189–215, 2020.
- Chai, T. and Draxler, R. R. Root mean square error (rmse) or mean absolute error (mae)?—arguments against avoiding rmse in the literature. *Geoscientific model development*, 7(3):1247–1250, 2014.
- Chen, J., Chen, S., Fu, R., Li, D., Jiang, H., Wang, C., Peng, Y., Jia, K., and Hicks, B. J. Remote sensing big data for water environment monitoring: current status, challenges, and future prospects. *Earth’s Future*, 10(2): e2021EF002289, 2022.
- Chen, T. Xgboost: extreme gradient boosting. *R package version 0.4-2*, 1(4), 2015.
- Cheng, G., Xie, X., Han, J., Guo, L., and Xia, G.-S. Remote sensing image scene classification meets deep learning: Challenges, methods, benchmarks, and opportunities. *IEEE Journal of Selected Topics in Applied Earth Observations and Remote Sensing*, 13:3735–3756, 2020.
- Chicco, D. and Jurman, G. The advantages of the matthews correlation coefficient (mcc) over f1 score and accuracy in binary classification evaluation. *BMC genomics*, 21: 1–13, 2020.
- Dalei, H., Qing, X., Jianguang, W., Dongqin, Y., Xiaodan, W., Xingwen, L., and Shengbiao, W. Advances in up-scaling methods of quantitative remote sensing. *National Remote Sensing Bulletin*, 22(3):408–423, 2021.
- Deng, J., Dong, W., Socher, R., Li, L.-J., Li, K., and Fei-Fei, L. Imagenet: A large-scale hierarchical image database. In *2009 IEEE conference on computer vision and pattern recognition*, pp. 248–255. Ieee, 2009.
- Diaz-Gonzalez, F. A., Vuelvas, J., Correa, C. A., Vallejo, V. E., and Patino, D. Machine learning and remote sensing techniques applied to estimate soil indicators—review. *Ecological Indicators*, 135:108517, 2022.
- Dong, C., Loy, C. C., He, K., and Tang, X. Image super-resolution using deep convolutional networks. *IEEE transactions on pattern analysis and machine intelligence*, 38(2):295–307, 2015.
- Gardner, M. W. and Dorling, S. Artificial neural networks (the multilayer perceptron)—a review of applications in the atmospheric sciences. *Atmospheric environment*, 32 (14-15):2627–2636, 1998.
- Gorelick, N., Hancher, M., Dixon, M., Ilyushchenko, S., Thau, D., and Moore, R. Google earth engine: Planetary-scale geospatial analysis for everyone. *Remote sensing of Environment*, 202:18–27, 2017.
- Hecht-Nielsen, R. Theory of the backpropagation neural network. In *Neural networks for perception*, pp. 65–93. Elsevier, 1992.
- Himeur, Y., Rimal, B., Tiwary, A., and Amira, A. Using artificial intelligence and data fusion for environmental monitoring: A review and future perspectives. *Information Fusion*, 86:44–75, 2022.

- Hochreiter, S. Long short-term memory. *Neural Computation MIT-Press*, 1997.
- Hore, A. and Ziou, D. Image quality metrics: Psnr vs. ssim. In *2010 20th international conference on pattern recognition*, pp. 2366–2369. IEEE, 2010.
- Kidd, C., Takayabu, Y. N., Skofronick-Jackson, G. M., Huffman, G. J., Braun, S. A., Kubota, T., and Turk, F. J. The global precipitation measurement (gpm) mission. *Satellite Precipitation Measurement: Volume 1*, pp. 3–23, 2020.
- Kleyko, D., Rahimi, A., Rachkovskij, D. A., Osipov, E., and Rabaey, J. M. Classification and recall with binary hyperdimensional computing: Tradeoffs in choice of density and mapping characteristics. *IEEE transactions on neural networks and learning systems*, 29(12):5880–5898, 2018.
- Kucharczyk, M. and Hugenholtz, C. H. Remote sensing of natural hazard-related disasters with small drones: Global trends, biases, and research opportunities. *Remote Sensing of Environment*, 264:112577, 2021.
- Lai, W.-S., Huang, J.-B., Ahuja, N., and Yang, M.-H. Deep laplacian pyramid networks for fast and accurate super-resolution. In *Proceedings of the IEEE conference on computer vision and pattern recognition*, pp. 624–632, 2017.
- Le, M.-H., Zhang, R., Nguyen, B. Q., Bolten, J. D., Lakshmi, V., et al. Robustness of gridded precipitation products for vietnam basins using the comprehensive assessment framework of rainfall. *Atmospheric Research*, 293:106923, 2023.
- Li, J., Hong, D., Gao, L., Yao, J., Zheng, K., Zhang, B., and Chanussot, J. Deep learning in multimodal remote sensing data fusion: A comprehensive review. *International Journal of Applied Earth Observation and Geoinformation*, 112:102926, 2022.
- Liang, J., Cao, J., Sun, G., Zhang, K., Van Gool, L., and Timofte, R. Swinir: Image restoration using swin transformer. In *Proceedings of the IEEE/CVF international conference on computer vision*, pp. 1833–1844, 2021.
- Liang, S. *Quantitative remote sensing of land surfaces*. John Wiley & Sons, 2005.
- Lim, B., Son, S., Kim, H., Nah, S., and Mu Lee, K. Enhanced deep residual networks for single image super-resolution. In *Proceedings of the IEEE conference on computer vision and pattern recognition workshops*, pp. 136–144, 2017.
- Liu, Y., Ding, L., Chen, C., and Liu, Y. Similarity-based unsupervised deep transfer learning for remote sensing image retrieval. *IEEE Transactions on Geoscience and Remote Sensing*, 58(11):7872–7889, 2020.
- Ma, H., Zeng, J., Zhang, X., Fu, P., Zheng, D., Wigneron, J.-P., Chen, N., and Niyogi, D. Evaluation of six satellite- and model-based surface soil temperature datasets using global ground-based observations. *Remote Sensing of Environment*, 264:112605, 2021.
- Ma, L., Liu, Y., Zhang, X., Ye, Y., Yin, G., and Johnson, B. A. Deep learning in remote sensing applications: A meta-analysis and review. *ISPRS journal of photogrammetry and remote sensing*, 152:166–177, 2019.
- Mahrad, B. E., Newton, A., Icely, J. D., Kacimi, I., Abalansa, S., and Snoussi, M. Contribution of remote sensing technologies to a holistic coastal and marine environmental management framework: a review. *Remote Sensing*, 12(14):2313, 2020.
- Messina, G. and Modica, G. Twenty years of remote sensing applications targeting landscape analysis and environmental issues in olive growing: A review. *Remote Sensing*, 14(21):5430, 2022.
- Moraux, A., Dewitte, S., Cornelis, B., and Munteanu, A. Deep learning for precipitation estimation from satellite and rain gauges measurements. *Remote Sensing*, 11(21):2463, 2019.
- Nasir, I. M., Bibi, A., Shah, J. H., Khan, M. A., Sharif, M., Iqbal, K., Nam, Y., and Kadry, S. Deep learning-based classification of fruit diseases: An application for precision agriculture. *Comput. Mater. Contin.*, 66(2):1949–1962, 2021.
- Parker, J. R. *Algorithms for image processing and computer vision*. John Wiley & Sons, 2010.
- Prodhan, F. A., Zhang, J., Hasan, S. S., Sharma, T. P. P., and Mohana, H. P. A review of machine learning methods for drought hazard monitoring and forecasting: Current research trends, challenges, and future research directions. *Environmental modelling & software*, 149:105327, 2022.
- Pu, R.-l. and Gong, P. Hyperspectral remote sensing and its applications. *Higher Education, Beijing*, 8, 2000.
- Ronneberger, O., Fischer, P., and Brox, T. U-net: Convolutional networks for biomedical image segmentation. In *Medical image computing and computer-assisted intervention—MICCAI 2015: 18th international conference, Munich, Germany, October 5-9, 2015, proceedings, part III 18*, pp. 234–241. Springer, 2015.
- Sainath, T. N., Vinyals, O., Senior, A., and Sak, H. Convolutional, long short-term memory, fully connected deep neural networks. In *2015 IEEE international conference*

- on acoustics, speech and signal processing (ICASSP), pp. 4580–4584. Ieee, 2015.
- Salcedo-Sanz, S., Ghamisi, P., Piles, M., Werner, M., Cuadra, L., Moreno-Martínez, A., Izquierdo-Verdiguier, E., Muñoz-Marí, J., Mosavi, A., and Camps-Valls, G. Machine learning information fusion in earth observation: A comprehensive review of methods, applications and data sources. *Information Fusion*, 63:256–272, 2020.
- Schneider, A., Friedl, M. A., and Potere, D. Mapping global urban areas using modis 500-m data: New methods and datasets based on ‘urban ecoregions’. *Remote sensing of environment*, 114(8):1733–1746, 2010.
- Segal, M. R. Machine learning benchmarks and random forest regression. 2004.
- Shi, W., Caballero, J., Huszár, F., Totz, J., Aitken, A. P., Bishop, R., Rueckert, D., and Wang, Z. Real-time single image and video super-resolution using an efficient sub-pixel convolutional neural network. In *Proceedings of the IEEE conference on computer vision and pattern recognition*, pp. 1874–1883, 2016.
- Singh, P., Pandey, P. C., Petropoulos, G. P., Pavlides, A., Srivastava, P. K., Koutsias, N., Deng, K. A. K., and Bao, Y. Hyperspectral remote sensing in precision agriculture: Present status, challenges, and future trends. In *Hyperspectral remote sensing*, pp. 121–146. Elsevier, 2020.
- Spadoni, G. L., Cavalli, A., Congedo, L., and Munafò, M. Analysis of normalized difference vegetation index (ndvi) multi-temporal series for the production of forest cartography. *Remote Sensing Applications: Society and Environment*, 20:100419, 2020.
- Tmušić, G., Manfreda, S., Aasen, H., James, M. R., Gonçalves, G., Ben-Dor, E., Brook, A., Polinova, M., Arranz, J. J., Mészáros, J., et al. Current practices in uas-based environmental monitoring. *Remote Sensing*, 12(6):1001, 2020.
- Tsakiris, G. and Loucks, D. Adaptive water resources management under climate change: an introduction. *Water Resources Management*, 37(6):2221–2233, 2023.
- Tsatsaris, A., Kalogeropoulos, K., Stathopoulos, N., Louka, P., Tsanakas, K., Tsemlis, D. E., Krassanakis, V., Petropoulos, G. P., Pappas, V., and Chalkias, C. Geoinformation technologies in support of environmental hazards monitoring under climate change: An extensive review. *ISPRS International Journal of Geo-Information*, 10(2): 94, 2021.
- Wang, X., Yu, K., Wu, S., Gu, J., Liu, Y., Dong, C., Qiao, Y., and Change Loy, C. Esrgan: Enhanced super-resolution generative adversarial networks. In *Proceedings of the European conference on computer vision (ECCV) workshops*, pp. 0–0, 2018.
- Wang, Y., Meili, N., and Fatichi, S. Evidence and controls of the acceleration of the hydrological cycle over land. *Water Resources Research*, 59(8):e2022WR033970, 2023.
- Wang, Z., Bovik, A. C., Sheikh, H. R., and Simoncelli, E. P. Image quality assessment: from error visibility to structural similarity. *IEEE transactions on image processing*, 13(4):600–612, 2004.
- Willmott, C. J. and Matsuura, K. Advantages of the mean absolute error (mae) over the root mean square error (rmse) in assessing average model performance. *Climate research*, 30(1):79–82, 2005.
- Willmott, C. J., Robeson, S. M., and Matsuura, K. A refined index of model performance. *International Journal of climatology*, 32(13):2088–2094, 2012.
- Wu, H., Yang, Q., Liu, J., and Wang, G. A spatiotemporal deep fusion model for merging satellite and gauge precipitation in china. *Journal of Hydrology*, 584:124664, 2020.
- Wu, X., Xiao, Q., Wen, J., You, D., and Hueni, A. Advances in quantitative remote sensing product validation: Overview and current status. *Earth-Science Reviews*, 196: 102875, 2019.
- Xia, B., Zhang, Y., Wang, S., Wang, Y., Wu, X., Tian, Y., Yang, W., and Van Gool, L. Diffir: Efficient diffusion model for image restoration. In *Proceedings of the IEEE/CVF International Conference on Computer Vision*, pp. 13095–13105, 2023.
- Xu, H., Huang, W., Si, X., Li, X., Xu, W., Zhang, L., Song, Q., and Gao, H. Onboard spectral calibration and validation of the satellite calibration spectrometer on hy-1c. *Optics Express*, 30(15):27645–27661, 2022.
- Yuan, Q., Shen, H., Li, T., Li, Z., Li, S., Jiang, Y., Xu, H., Tan, W., Yang, Q., Wang, J., et al. Deep learning in environmental remote sensing: Achievements and challenges. *Remote sensing of Environment*, 241:111716, 2020.
- Zhang, K., Liang, J., Van Gool, L., and Timofte, R. Designing a practical degradation model for deep blind image super-resolution. In *Proceedings of the IEEE/CVF International Conference on Computer Vision*, pp. 4791–4800, 2021.
- Zhao, Q., Yu, L., Du, Z., Peng, D., Hao, P., Zhang, Y., and Gong, P. An overview of the applications of earth observation satellite data: impacts and future trends. *Remote Sensing*, 14(8):1863, 2022.

Zhou, L. and Liu, L. Enhancing dynamic flood risk assessment and zoning using a coupled hydrological-hydrodynamic model and spatiotemporal information weighting method. *Journal of Environmental Management*, 366:121831, 2024.